Check for updates

Dual-emission center ratiometric optical thermometer based on Bi^{3+} and Mn^{4+} co-doped $SrGd_2Al_2O_7$ phosphor

Yi Yu, [ID] †*[ab] Kai Shao,†[ab] Chonghui Niu,[ab] Mingjie Dan,[ab] Yingying Wang,[a] Xiourong Zhu, [ID] [abc] Xianke Zhang [ID] [a] and Yeqing Wang*[d]

In recent years, more and more attention has been paid to optical temperature sensing, and how to improve its accuracy is the most important issue. Herein, a new temperature sensing material, $SrGd_2Al_2O_7$:Bi^{3+},Mn^{4+}, based on fluorescence intensity ratio was designed in this work. It has both blue-purple and red luminescence under 300 nm excitation, and the dual-emitting centers with distinct colors, the different thermal sensitivities of Bi^{3+} and Mn^{4+}, and the energy transfer between Bi^{3+} and Mn^{4+} give it excellent signal resolution and accurate temperature detection. The S_a of $SrGd_2Al_2O_7$:$0.04Bi^{3+}$,$0.003Mn^{4+}$ phosphor reaches a maximum value of 8.573% K^{-1} at 473 K, and the corresponding S_r is 1.927% K^{-1}, both of which are significantly better than those of most other reported optical temperature sensing materials. Taking all the results into account, the $SrGd_2Al_2O_7$:$0.04Bi^{3+}$,$0.003Mn^{4+}$ phosphor can be regarded as a prominent FIR-type temperature sensing material.

1. Introduction

Temperature is a physical quantity that shows how hot or cold something is. It is a fundamental and important physical quantity in daily life, industrial applications, scientific research, etc. Currently, thermometers can be divided mainly into contact type and non-contact type. The working principle of the contact type is based mainly on the thermocouple characteristics or the Seebeck effect, the latter relying on temperature-dependent optical properties.[1]

Traditional contact thermometers have limitations in application to biological tissue, or in a corrosive or strongly magnetic environment. For example, in the outbreak of the novel coronavirus pneumonia from December 2019, the virus is highly contagious, and the use of contact temperature measuring instruments greatly increases the risk of virus transmission, so non-contact measurement is an ideal choice to resolve this problem. Even in a variety of other fields, non-contact temperature measurement is still preferred. However, although many kinds of non-contact temperature sensors are

emerging in the market at present, most of them are greatly affected by the environment, resulting in low measurement accuracy and large error, which makes the test results less repeatable. An optical temperature sensor can not only easily realize non-contact measurement, but also maintain high measurement accuracy in a special measurement environment. It also has incomparable advantages over traditional contact temperature sensors in terms of volume, response speed and sensitivity. Therefore, research on optical temperature sensors has attracted more and more attention.[2]

Owing to their abundant and complex energy levels and temperature-sensitive optical behavior, lanthanide-ion-based fluorescence intensity ratio (FIR)-type temperature measurement materials are taking a leading role in the field of temperature sensing materials. However, their band gaps are often relatively narrow, leading to problems, including overlap of two transmitted signals, large detection deviation and poor resolution. These drawbacks in turn limit their ability to measure temperature with high accuracy.[3,4] In order to overcome these shortcomings, temperature sensing materials based on multiple emission centers with different thermal sensitivities, such as rare earth/rare earth (Re/Re) or transition metal/rare earth (Tr/Re) ion co-doped materials, have been designed in recent years. Among these co-doped materials, Eu^{3+}/Tb^{3+}, Eu^{3+}/Bi^{3+}, and Eu^{3+}/Dy^{3+} groups have revealed excellent temperature sensing ability.[5–7] However, there are few reports on temperature sensing materials doped by double transition group metal elements. The luminescence properties of Bi^{3+} ions are easily affected by the crystal field environment where the ions reside. Based on their adjustable luminescence, Bi^{3+} ions are often selected as efficient

[a]School of Physics and Electronic Information, Gannan Normal University, Ganzhou 341000, China. E-mail: yuyignnu@163.com

[b]Advanced Energy Storage & Photoelectric Materials Research Center, Gannan Normal University, Ganzhou 341000, China

[c]Shanghai Key Laboratory of Special Artificial Microstructure Materials & Technology, Department of Physics, Tongji University, Shanghai 200092, China

[d]Department of Applied Physics, East China Jiaotong University, Nanchang, 330013, Jiangxi, China. E-mail: jxdxmeng@126.com

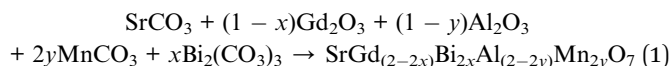† These authors contributed equally to this work.

sensitizers for activator ions. For instance, a lot of studies about enhancing the luminescent properties of Eu^{3+}, Pr^{3+}, and Tb^{3+} by means of co-doping Bi^{3+} ions as a sensitizer have been reported.[6,8,9] On the other hand, Bi^{3+} itself can usually emit blue-purple light and its intensity depends on temperature, which makes it suitable for temperature sensing by measuring the fluorescent intensity at different temperatures. But this mono-band method for temperature sensing often suffers drawbacks, such as relatively low accuracy, low signal resolution and larger error. Compared to this method, the dual-emission center ratiometric method is advantageous. Hence, apart from the blue-purple emission band from Bi^{3+}, another ion should be selected to offer a different emission band. Because of its preeminent optical properties, Mn^{4+}-based red-emitting phosphors were regarded as promising fluorescent materials. More and more Mn^{4+}-doped phosphors have gained a lot of attention recently. The good match between the $^4T_{2g}$ state of Mn^{4+} and the $^3P_1$ state of Bi^{3+} provides a strategy for designing a temperature sensing material based on the fluorescent intensity ratio of the blue-purple emission to red emission. Therefore, we designed a new type of thermometer based on energy transfer between Bi^{3+} and Mn^{4+} using $SrGd_2Al_2O_7$ (SGAO) as a matrix. The physical and chemical properties of SGAO are stable, and the Gd(Sr) atoms are distributed at two different sites, forming nine- and twelve-fold coordinated polyhedrons, which provides a good crystal field environment for Bi^{3+} ion substitution. In addition, the $[AlO_6]$ octahedron is very suitable for Mn^{4+} ion substitution and far-red emission (Fig. 1). Therefore, the emission of Bi^{3+} ions and Mn^{4+} ions is very easy to distinguish, and it can be predicted that this temperature sensing material should have good signal detection ability. Moreover, because of the energy transfer from sensitizer Bi^{3+} ions to activator Mn^{4+} ions, it is more suitable for design as an FIR-based dual-emission center temperature sensing material.

2. Experimental

2.1 Synthesis

A series of SGAO:xBi^{3+},yMn^{4+} ($0.01 \leq x \leq 0.075$; $0 \leq y \leq 0.01$) phosphors were prepared by a high-temperature solid-state reaction. Raw materials $SrCO_3$ (99.5%), Gd_2O_3 (99.99%), Al_2O_3

(99.99%), $MnCO_3$ (99.99%), Al_2O_3 (99.99%), $Bi_2(CO_3)_3$ (99.99%) were all purchased from Aladdin Reagents. They were stoichiometrically weighted according to the chemical equation:

$$SrCO_3 + (1 - x)Gd_2O_3 + (1 - y)Al_2O_3$$
$$+ 2yMnCO_3 + xBi_2(CO_3)_3 \rightarrow SrGd_{(2-2x)}Bi_{2x}Al_{(2-2y)}Mn_{2y}O_7 \quad (1)$$

where x and y represent the doping concentrations of Bi^{3+} ions and Mn^{4+} ions, respectively. The mixtures were thoroughly ground for about 40 minutes and then transferred into a corundum crucible for calcining. A muffle furnace was adopted and the temperature was increased to 1550 °C at a heating rate of 3 °C min^{-1} in air. The temperature was kept constant for 10 hours. After natural cooling to room temperature, the products were ultimately obtained.

2.2 Properties measurements

XRD diffraction measurement was conducted on a high-resolution X-ray powder diffractometer (Rigaku Ultima-IV) with Cu Kα radiation as the radiative source to analyze the phase of the SGAO:xBi^{3+},yMn^{4+} ($0.01 \leq x \leq 0.075$; $0 \leq y \leq 0.01$) phosphors. The signals were recorded in the range of 20–65° at a rate of 2° min^{-1}. A scanning electron microscope (JSM-6700F) was used to obtain the surface morphology information for the samples. To measure the PL and PLE spectra, a fluorescence spectrometer (Hitachi-2500) equipped with a 150 W xenon lamp as the light source was adopted. The measurement of temperature-dependent emission spectra and decay curves were implemented on an Edinburgh FLS 980 spectrometer. The temperature fluctuated from 303 K to 473 K.

3. Results and discussion

3.1 Phase and morphology analysis

The XRD patterns of all SGAO:Bi^{3+} and SGAO:Bi^{3+},Mn^{4+} samples are shown in Fig. 2, accompanied by the standard pattern for the pure phase of SGAO compound (PDF# 76-0095). All the diffraction patterns are obviously very well matched with the standard PDF card for pure SGAO compound without the appearance of any additional diffraction peaks, indicating that all the samples obtained have the same phase as the SGAO compound. In order to determine the substitution position of dopant ions, the value of the percentage difference of radius (D_r) can be calculated with the following equation:[10]

$$D_r = \frac{[R_m(CN) - R_d(CN)]}{R_m(CN)} \times 100\% \quad (2)$$

where R_m and R_d are the radii of host ion and doping ion, respectively, and CN refers to the coordination number of the corresponding ions. The smaller the value of D_r, the easier it is to replace the host ions. According to eqn (2), the D_r values for the cases of a Bi^{3+} ion replacing a Gd^{3+} ion and an Al^{3+} ion are 2.70% and 111.11%, and the D_r values for the cases of an Mn^{4+} ion replacing a Gd^{3+} ion and an Al^{3+} ion are 52.25% and 1.85%, respectively. Therefore, it is rational to claim that Bi^{3+} ions replace Gd^{3+} ions and Mn^{4+} ions occupy the Al^{3+} sites.
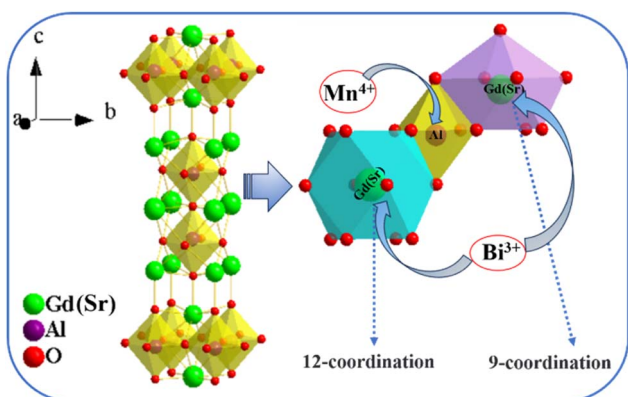

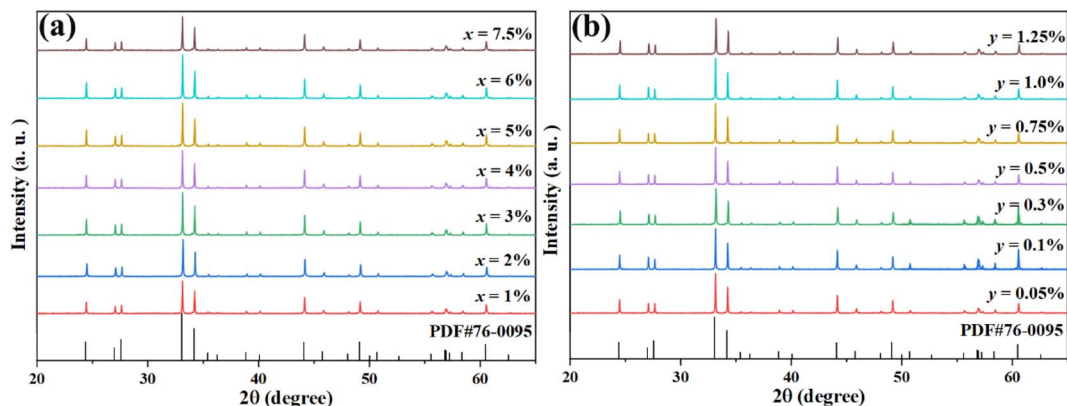**Fig. 1** Structure framework of SGAO compound and Gd(Sr)–O, Al–O polyhedrons.

Fig. 2 XRD patterns of (a) SGAO:xBi^{3+} (0.01 ≤ x ≤ 0.075) and (b) SGAO:0.04Bi^{3+},yMn^{4+} (0.0005 ≤ y ≤ 0.0125).

Fig. 3(a) and (b) show the SEM images of the SGAO:0.04-Bi^{3+},0.003Mn^{4+} phosphor taken at different magnification rates. It can be seen from the figures that the morphology of the samples is irregular and there is a certain degree of agglomeration, which is a common phenomenon for materials synthesized through a traditional high-temperature solid-state reaction. The size of phosphor is estimated to be about 1–5 μm.

3.2 Photoluminescence properties

In order to investigate the photoluminescence characteristics of Bi^{3+} and Mn^{4+} ions in the SGAO host, the photoluminescence excitation (PLE) and photoluminescence (PL) spectra of SGAO:Bi^{3+} and SGAO:Mn^{4+} were performed and the results are shown in Fig. 4(a) and (b), respectively. The PLE spectrum of SGAO:Bi^{3+}, in a wavelength range of 265–335 nm with the maximum peak at 300 nm is the typical electronic transition band of Bi^{3+}, which corresponds to the transition from ground-state $^1S_0$ to excited-state $^3P_1$. Excited at 300 nm, the emission spectrum of SGAO:Bi^{3+} has only a single band with a wavelength range of 350–510 nm, and the peak is located at about 404 nm. This broad emission band is ascribed to the $^3P_1$ → $^1S_0$

transition of Bi^{3+}.[11] The PLE spectrum of SGAO:Mn^{4+} consists of two bands in the wavelength ranges of 270–440 nm and 440–550 nm, with their corresponding peaks of 340 nm and 487 nm. Under excitation at 340 nm, SGAO:Mn^{4+} shows a single emission band in the wavelength range of 670–760 nm, which corresponds to the ^2E_g → $^4A_{2g}$ transition of an Mn^{4+} ion in an [AlO$_6$] octahedral environment. Comparing the emission band of a Bi^{3+} ion and excitation band of an Mn^{4+} ion, it is intriguing to note that they overlap significantly with each other, as shown in Fig. 4(b), indicating a rational strategy in which the intensity of luminescence of Mn^{4+} ions can be enhanced by Bi^{3+} ions, which play the role of sensitization.[10,12]

Fig. 5(a) shows the PL spectra of SGAO:xBi^{3+} (0.01 ≤ x ≤ 0.075) over a range of 350–510 nm. With the change in doped Bi^{3+} ion concentration, all the PL spectra keep the same shapes without obvious red shift or blue shift, and they are centered at 404 nm. However, the emission intensity fluctuates greatly with variation in the concentration of Bi^{3+} ions. The inset in Fig. 5(a) shows the variation in emission intensities at 404 nm with the increase in Bi^{3+} concentration. As one can see, the emission intensity of the SGAO:xBi^{3+} (0.01 ≤ x ≤ 0.075) phosphor first
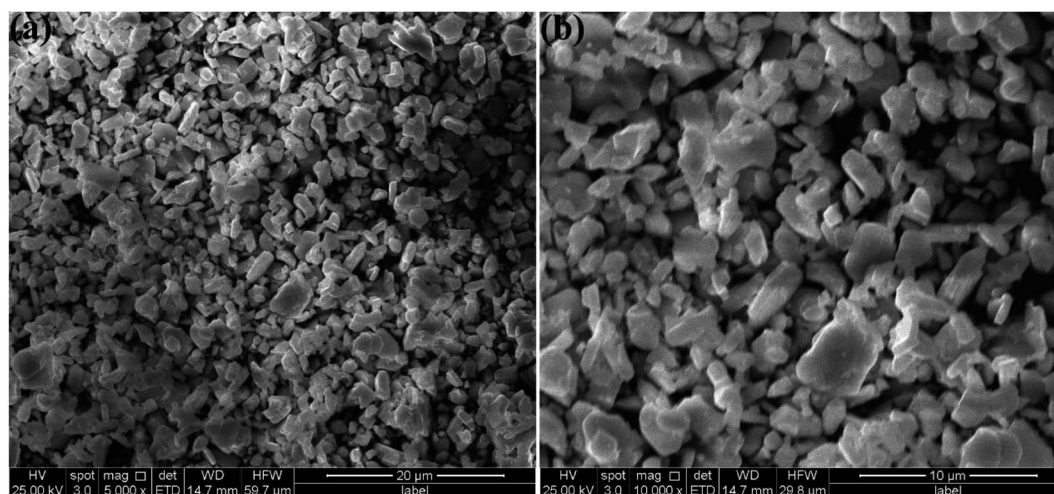

Fig. 3 SEM images of SGAO:0.04Bi^{3+},0.003Mn^{4+} phosphors at low (a) and high (b) magnification.
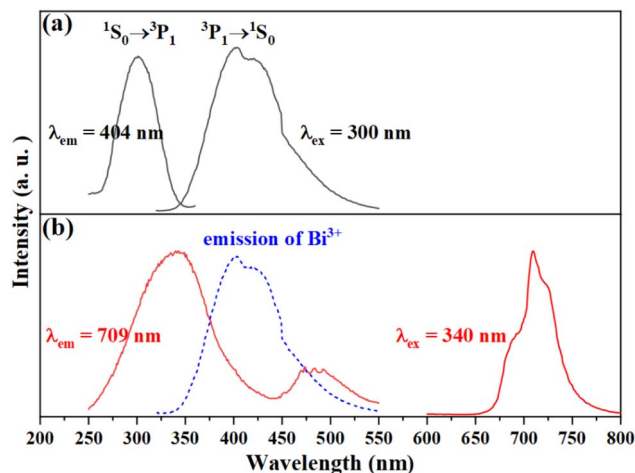
Fig. 4 Excitation (PLE) and emission spectra (PL) of (a) SGAO:Bi^{3+} and (b) SGAO:Mn^{4+}.

increases at lower doping concentration and then decreases at higher doping concentration. It reaches its maximum altitude when $x = 0.04$, indicating that the optimized concentration of Bi^{3+} ions should be 4 at%. To explore the quenching mechanism of the concentration of the SGAO:Bi^{3+} phosphor, the critical distance (R_c) can be calculated as follows:[13]

$$R_c \approx \left[\frac{3V}{4\pi x_c N}\right]^{\frac{1}{3}} \quad (3)$$

where V is the volume of a unit cell, N means the number of substitutable cations in the host matrix in a unit cell, and x_c represents the critical concentration of activator ions. In the SGAO matrix, $V = 271.56$ Å^3, $x_c = 0.04$, $N = 4$. Thus, the value of R_c was calculated to be 14.8 Å, much greater than 5 Å. Therefore, it can be assumed that the quenching mechanism is the multipole interaction mechanism. For a further determination of the type of interaction mechanism between Bi^{3+} ions, the following formula based on Dexter's theory was adopted:[14]

$$\log\left(\frac{I}{x}\right) = A - \frac{Q}{3}\log x \quad (4)$$

where I is the emission intensity, x represents the doping concentration, A denotes a constant, and $Q = 6$, 8, and 10 correspond to dipole–dipole, dipole–quadrupole, and quadrupole–quadrupole interactions, respectively. Fig. 5(b) shows $\log(I/x)$ as a function of $\log(x)$. By the linear fitting method, the slope is determined to be -1.16. Further calculation shows that Q is 3.48, which is closer to 6, indicating that the dipole–dipole interaction between Bi^{3+} ions in the SGAO matrix is responsible for the concentration quenching.

With the concentration of Bi^{3+} kept constant at 4 at%, samples with Mn^{4+} co-doped at different concentrations were fabricated and the effect of Mn^{4+} concentration on the luminescence properties was investigated. Fig. 6(a) shows the broad emission band of SGAO:0.04Bi^{3+}, yMn^{4+} ($0 \leq y \leq 0.01$) phosphors corresponding to the $^3P_1 \rightarrow {}^1S_0$ transition of Bi^{3+} measured in a 350–510 nm range,[15] as well as the emission band in the 670–760 nm ascribed to the $^2E_g \rightarrow {}^4A_{2g}$ transition of Mn^{4+}.[16] Fig. 6(b) depicts the luminescence intensity of Bi^{3+} and Mn^{4+} ions depending on the different concentrations of Mn^{4+} ions. With the increase in Mn^{4+} concentration, the emission intensity of Mn^{4+} ions increases first and then decreases. And when $y = 0.003$, it reaches the summit. In contrast, the emission intensity of Bi^{3+} ions decreases along with the rise in Mn^{4+} ion concentration, which is because of the existence of energy transfer process from Bi^{3+} ion to Mn^{4+} ion. The reason for the phenomenon that the emission intensity of Mn^{4+} ions increases first and then decreases can be ascribed to the integrative effects of energy transfer from Bi^{3+} to Mn^{4+} ions and the concentration quenching of the Mn^{4+} ion itself. Evidence for this hypothesis can be extracted from the fact that the optimized concentration of Mn^{4+} ions, namely 0.3 at%, rather than 0.1 at% which was reported in our very recent studies into the Mn^{4+}-single doped SGAO phosphor.[17] As such, this change in the optimum concentration of Mn^{4+} ions from 0.1 at% in SGAO to 0.3 at% in SGAO:0.04Bi^{3+},Mn^{4+} demonstrates that the procedure of energy transfer from Bi^{3+} to Mn^{4+} ions does occur in the Bi^{3+} and Mn^{4+} co-doped SGAO phosphor. Furthermore, when $0.001 \leq y \leq 0.003$, the positive effect of energy transfer from Bi^{3+} to Mn^{4+} ions is stronger than the negative effect of
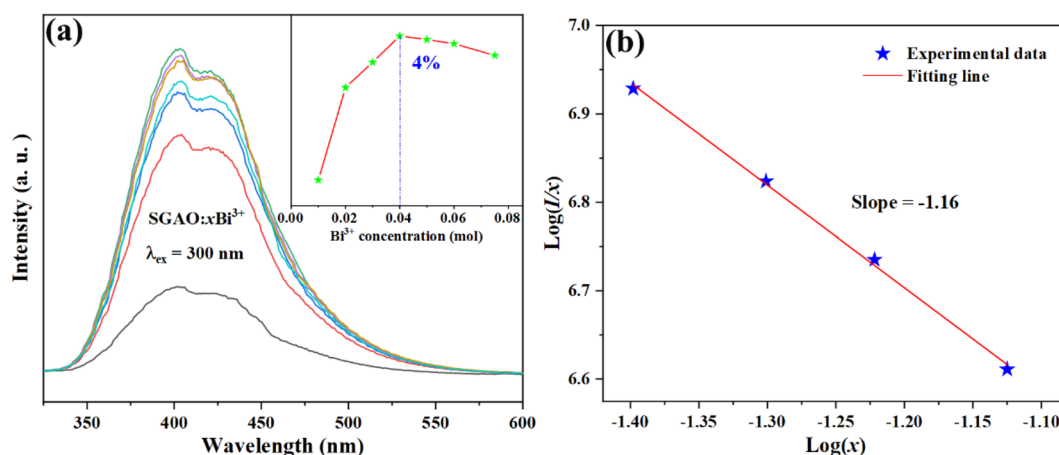

Fig. 5 (a) Emission spectra of SGAO:xBi^{3+} ($0.01 \leq x \leq 0.075$) phosphors; (b) $\log(I/x)$ dependence on $\log(x)$.
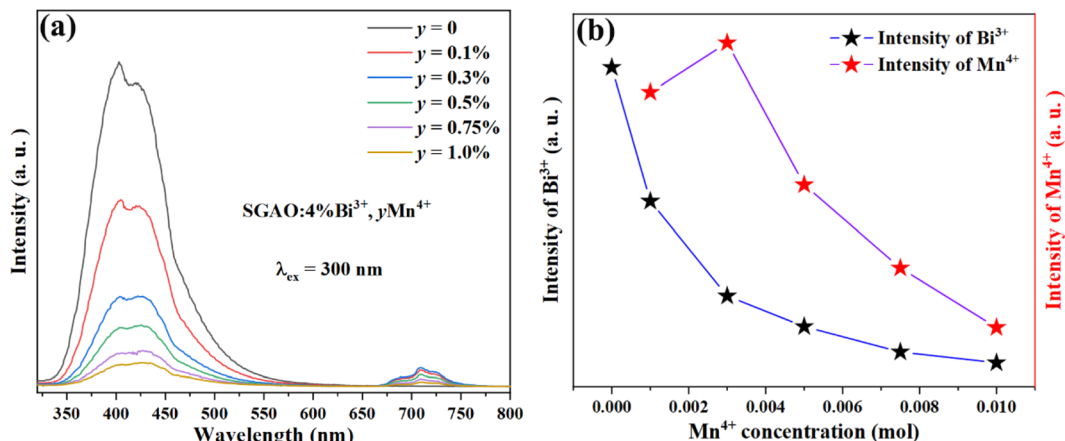
Fig. 6 (a) Emission spectra of phosphors SGAO:0.04Bi^{3+},yMn^{4+} (0 ≤ y ≤ 0.01). (b) The luminescence intensity of Bi^{3+} and Mn^{4+} ions vary with the doping concentration of Mn^{4+} ions.

Mn^{4+} ion concentration quenching. However, when y is larger than 0.003, the interaction between adjacent Mn^{4+} ions becomes much stronger, which gives the significant effect of emission weakness by concentration quenching the lead role in competition with the energy transfer process.

As the decay characteristic of the Bi^{3+} and Mn^{4+} ions is an effective way to reveal the mechanism of energy transfer between the two kinds of ions, the fluorescence lifetimes of Bi^{3+} in the series of SGAO:0.04Bi^{3+},yMn^{4+} (0 ≤ y ≤ 0.01) phosphors were measured. All the phosphors were excited at 300 nm and monitored at 404 nm and the decay curves are portrayed in Fig. 7. The decay curves were fitted with a double-exponential formula which can be expressed as follows:[18,19]

$$\begin{cases} I_t = I_0 + A_1 \exp\left(-\dfrac{t}{\tau_1}\right) + A_2 \exp\left(-\dfrac{t}{\tau_2}\right) \\ \tau_{ave} = \left(A_1\tau_1^2 + A_2\tau_2^2\right)/\left(A_1\tau_1 + A_2\tau_2\right) \end{cases} \quad (5)$$

where I_t is the luminescence intensity changing with time, A_1 and A_2 are constants, τ_1 and τ_2 represent the decay coefficients,
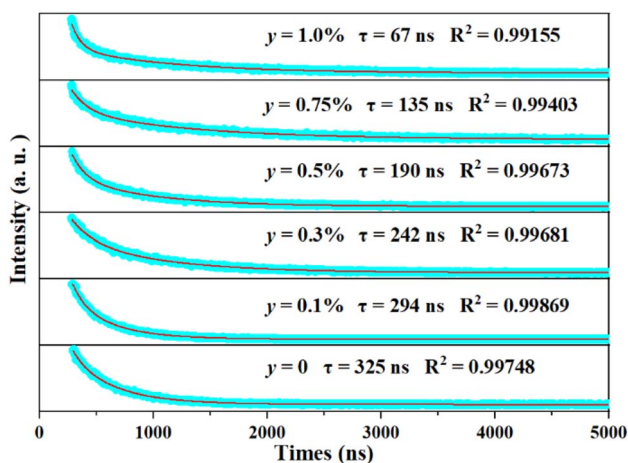
and τ_{ave} means the average fluorescence lifetimes. Based on this equation, the lifetimes of Bi^{3+} ions in the SGAO co-doped with Mn^{4+} were obtained. As anticipated, they continuously decrease with an increase in Mn^{4+} ion concentration, from 325 ns to 67 ns as y goes up from 0 to 0.01. In addition, the shrinkage of the lifetimes of Bi^{3+} ions become faster with the increase in y values. The reason for this is mainly because the higher the concentration of Mn^{4+} ions, the shorter the distance between Bi^{3+} ions and Mn^{4+} ions, and as a consequence, the energy transfer of Bi^{3+} → Mn^{4+} was boosted with higher efficiency and this obviously leads to the shortened luminescence lifetimes of Bi^{3+} ions. The efficiency of energy transfer from Bi^{3+} to Mn^{4+} can be calculated with the following formula:[20]

$$\eta_t = 1 - \frac{\tau}{\tau_0} \quad (6)$$

where τ_0 is the lifetime of Bi^{3+} ions when Mn^{4+} ions are absent, and τ is the lifetime when Mn^{4+} ions are co-doped with different concentrations. Therefore, the efficiencies for the SGAO:0.04Bi^{3+},yMn^{4+} (0.001 ≤ y ≤ 0.01) phosphors are 9.5%, 25.5%, 41.5%, 58.5%, and 79.4%, respectively. Interestingly, the efficiencies increase with a rise in Mn^{4+} ion concentration, and these results further demonstrate the aforementioned hypothesis.

According to the above results and analysis, the electron transition and energy transfer processes in the SGAO:0.04Bi^{3+},yMn^{4+} (0 ≤ y ≤ 0.01) phosphors are inferred, as shown in Fig. 8. When SGAO:0.04Bi^{3+},yMn^{4+} (0 ≤ y ≤ 0.01) phosphors are excited, a certain proportion of electrons from Bi^{3+} ions transfer from the ^{1}S$_0$ ground state to the ^{3}P$_1$, ^{3}P$_2$ and ^{1}P$_1$ excited states. Then they gradually relax from ^{1}P$_1$ to ^{3}P$_2$ and ^{3}P$_1$ states in a non-radiative process, resulting in energy consumption, which is regarded as an adverse effect. For the electrons in the ^{3}P$_1$ state, a proportion of them directly transit to the ^{1}S$_0$ ground state, accompanied by photon emission at the wavelength of 404 nm. Meanwhile, the rest of the electrons transfer their energy to the electrons in the ^{4}T$_{2g}$ state of neighboring Mn^{4+} ions and successively relax to the ^{2}E$_g$ state.
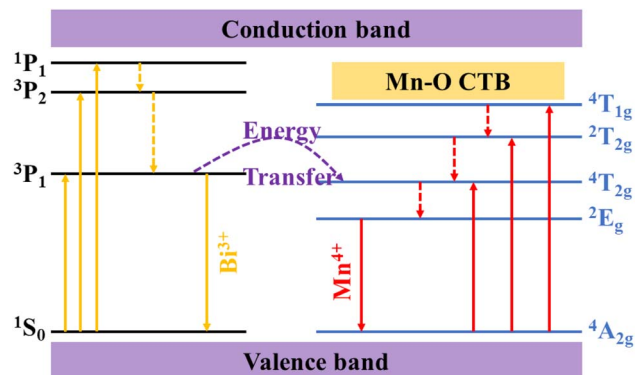

Fig. 7 Decay curve of SGAO:0.04Bi^{3+},yMn^{4+} (0 ≤ y ≤ 0.01) phosphors at room temperature.

Fig. 8 Electron transition and energy transfer of SGAO:Bi^{3+},Mn^{4+}.

For the Mn^{4+} ions themselves, electrons in the excited states $^4T_{1g}$, $^2T_{2g}$ and $^4T_{2g}$ will non-radiatively transit to the ^2E_g state. Therefore, with the assistance of Bi^{3+} ions, the red emission of Mn^{4+} ions at 709 nm corresponding to the $^2E_g \rightarrow {}^4A_{2g}$ transition can be achieved and the emission intensity is inevitably related to the concentration of Mn^{4+} ions.[21]

3.3 Temperature sensing behavior

Fig. 9(a) shows the emission spectra of SGAO:0.04-Bi^{3+},0.003Mn^{4+} phosphors at different temperatures within 303–473 K. The sample was excited at 300 nm. With an increase in temperature, both the emissions originated from Bi^{3+} ions at 404 nm and from Mn^{4+} ions at 709 nm decrease in turn, but the rates of descent are different. As shown in Fig. 9(b), in the temperature range of 303–393 K, the emission intensity of Bi^{3+} ions decreases faster, while in the temperature range of 393–473 K, the emission intensity of Mn^{4+} ions decreases faster. Considering this characteristic, it is rational to design a new type of optical temperature sensor based on the fluorescence intensity ratio in these two temperature ranges.

Fig. 10(a) shows the configuration coordinate diagram of Bi^{3+}. At room temperature, electrons transition to excited states of $^3P_2$ and $^1P_1$ by absorbing energy, and then relax to the $^3P_1$ state by non-radiative transition. Finally, electrons transition to the $^1S_0$ ground state and release photons, and the correlation path is expressed as (O $\rightarrow$ A $\rightarrow$ B $\rightarrow$ C $\rightarrow$ D $\rightarrow$ O). But at higher temperatures, due to the fluctuation of the energy band, intersection between excited-state $^3P_1$ and ground-state $^1S_0$ usually
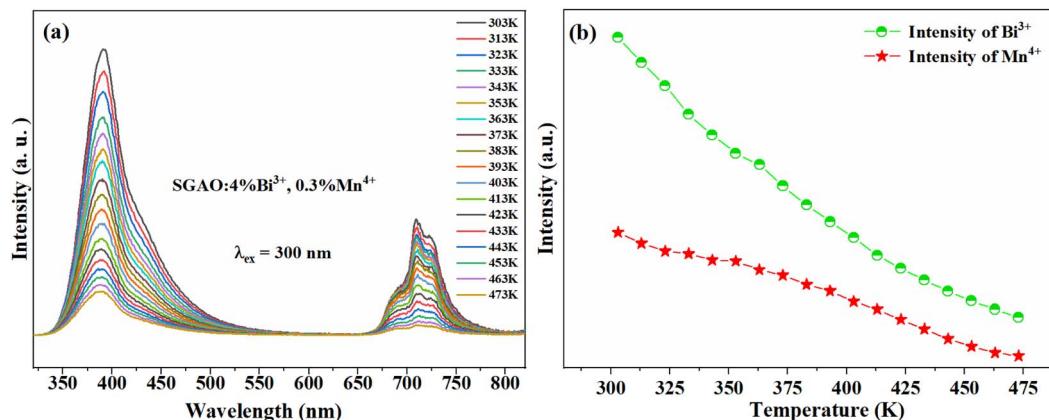

Fig. 9 (a) Temperature-dependent emission spectra of SGAO:0.04Bi^{3+},0.003Mn^{4+} phosphors. (b) The relationship between the emission intensity of Bi^{3+} (Mn^{4+}) and temperature.
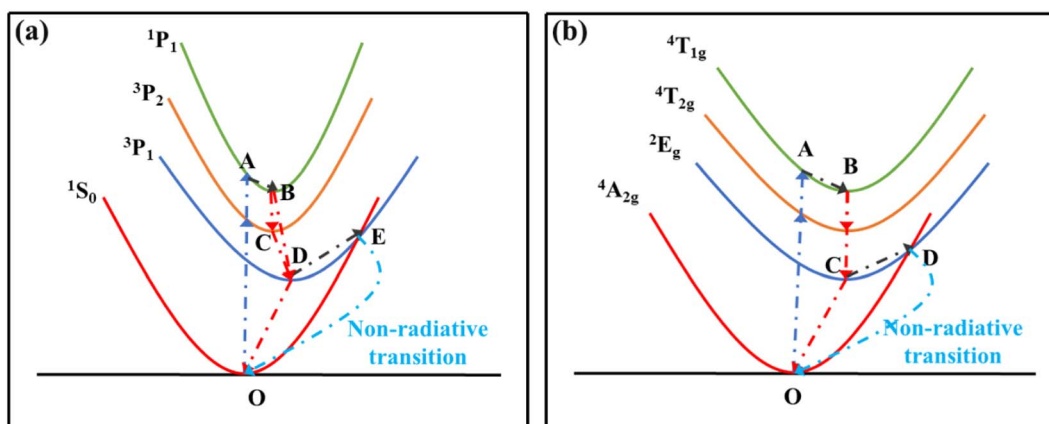

Fig. 10 Configuration coordinate diagrams of (a) Bi^{3+} and (b) Mn^{4+}.

occurs, denoted as point E in Fig. 10(a). Therefore, a proportion of electrons in the $^3P_1$ excited state will non-radiatively relax to ground-state $^1S_0$ through this intersection. The whole correlation path can be depicted as (O → A → B → C → D → E → O). In addition, the higher the temperature, the more frequently the electrons transit to the ground state through the non-radiative channel.[22] Obviously, this side effect will give rise to a weakness in emission intensity. When it comes to the Mn^{4+} ions, the mechanism of thermal quenching is similar to that of Bi^{3+} ions discussed above, and the configuration coordinate diagram of Mn^{4+} is shown in Fig. 10(b).

Based on Struck and Fonger theory, the relationship between photoluminescence intensity and temperature can be defined by the following formula:[23]

$$I_T = \frac{I_0}{1 + A \exp\left(-\dfrac{\Delta E}{k_B T}\right)} \qquad (7)$$

where I_T represents the photoluminescence intensity at a specified temperature, I_0 means the photoluminescence intensity at the initial temperature, T is the absolute temperature, A is a constant, k_B is the Boltzmann constant, and ΔE is the activation energy of the hot quenching process. According to the above formula, the relationship between FIR and T can be deduced as follows:[24–26]

$$
\begin{aligned}
\text{FIR} &= \frac{I_{Mn^{4+}}(T)}{I_{Bi^{3+}}(T)} \\
&= \frac{I_{0,Mn^{4+}}}{I_{0,Bi^{3+}}} \frac{1 + A_{Bi^{3+}} \exp\left(-\dfrac{E_{Bi^{3+}}}{k_B T}\right)}{1 + A_{Mn^{4+}} \exp\left(-\dfrac{E_{Mn^{4+}}}{k_B T}\right)} \approx B + D \exp\left(-\dfrac{\Delta E}{k_B T}\right)
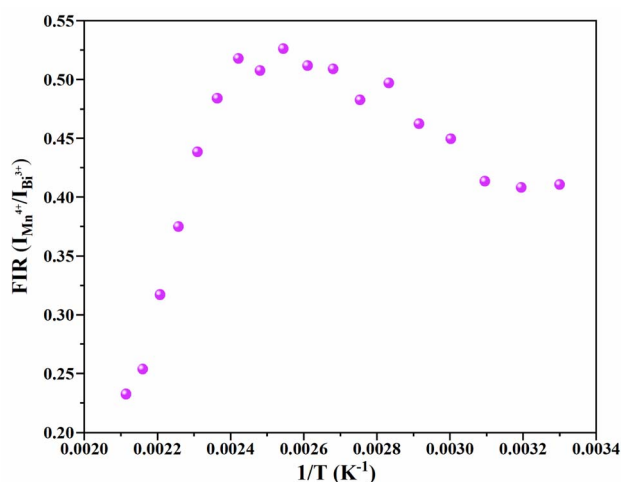\end{aligned}
\qquad (8)
$$

Fig. 11 Scatter diagram for the change in FIR ($I_{Mn^{4+}}/I_{Bi^{3+}}$) *versus* temperature from 303 K to 473 K.
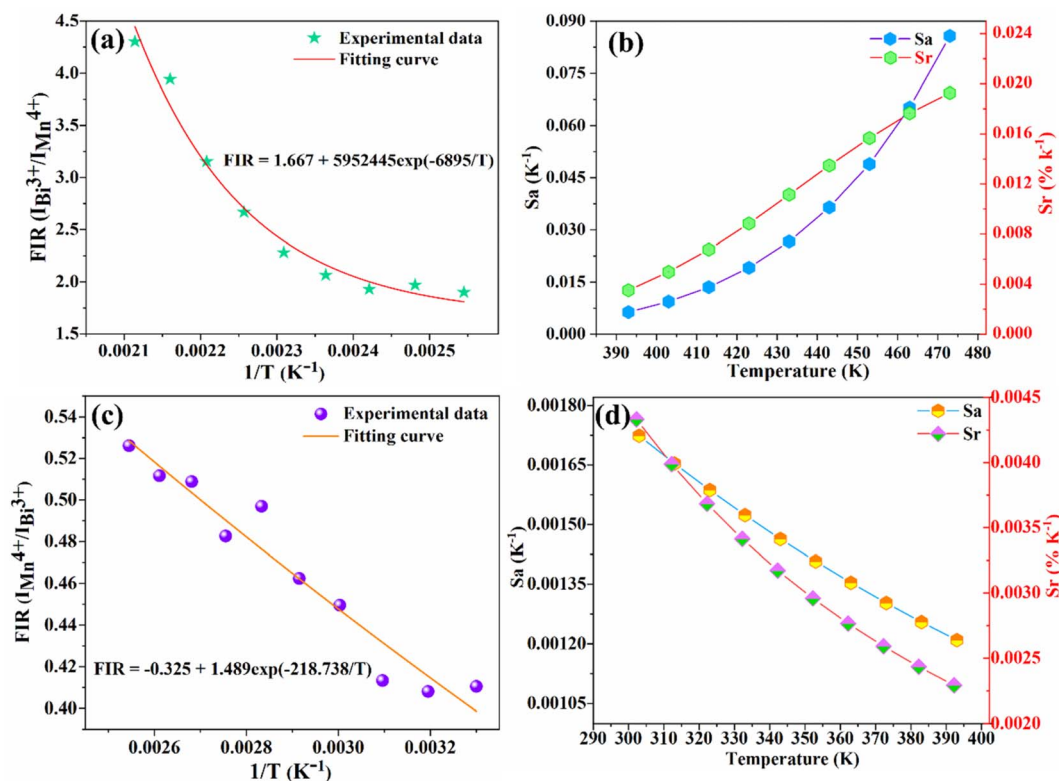

Fig. 12 (a) FIR ($I_{Bi^{3+}}/I_{Mn^{4+}}$) fitting curves in the temperature range of 393–473 K. (b) Curves of S_a and S_r with respect to temperature in the same range. (c) FIR ($I_{Mn^{4+}}/I_{Bi^{3+}}$) fitting curve in the temperature range of 303–393 K. (d) Curves of S_a and S_r with respect to temperature in the same range.

Table 1 S_a and S_r of different temperature measuring materials

Phosphors	Temperature range (K)	S_a (K^{-1})	S_r (K^{-1})	PLE peak (nm)	Ref.
LaAlO$_3$:Er^{3+}/Yb^{3+}	100–673	0.0048	0.0244	973	27
Sr$_4$Al$_{14}$O$_{25}$:Eu^{2+}	293–423	0.004	0.00624	373	28
ZnAl$_2$O$_4$:Cr^{3+}	80–310	<0.003	0.0025	310	29
LiAl$_{5(1-x)}$O$_8$:xCr^{3+}	200–600	0.015	0.0025	443	30
Ca$_{14}$Al$_{10}$Zn$_6$O$_{35}$:Bi^{3+}/Mn^{4+}	303–563	0.014	0.0121	340	31
Gd$_2$ZnTiO$_6$:Bi^{3+}/Mn^{4+}	313–473	0.168	0.024	420	32
SrGd$_2$Al$_2$O$_7$:Bi^{3+}/Mn^{4+}	393–473	0.0857	0.01927	300	This work

where B and D are related parameters. After the experimental data of FIR was fitted, a successive FIR curve could be obtained. Then the absolute sensitivity (S_a) that represents the change in FIR value when the temperature changes by 1 K can be calculated as follows:[25]

$$S_a = \left| \frac{\partial \mathrm{FIR}}{\partial T} \right| = D \exp\left(-\frac{\Delta E}{k_B T} \right) \times \frac{\Delta E}{k_B T^2} \qquad (9)$$

And the relative sensitivity (S_r) which represents the ratio of absolute sensitivity (S_a) to FIR can be calculated with the following formula:[26]

$$S_r = \left| \frac{1}{\mathrm{FIR}} \frac{\partial \mathrm{FIR}}{\partial T} \right| \times 100\% = \frac{D \exp\left(-\frac{\Delta E}{k_B T} \right)}{B + D \exp\left(-\frac{\Delta E}{k_B T} \right)} \times \frac{\Delta E}{k_B T^2} \qquad (10)$$

Fig. 11 depicts the scatter diagram for the FIR ($I_{\mathrm{Mn}^{4+}}/I_{\mathrm{Bi}^{3+}}$) of SGAO:0.04Bi^{3+},0.003Mn^{4+} phosphor as a function of temperature over the range 303–473 K and the corresponding range of the horizontal coordinate (1/T) is 0.0021–0.0033 K^{-1}. From this figure, one can see that the value of FIR shows a trend of first increasing and then decreasing and the turning point appears at 393 K. Thus, the fitting analysis was separately carried out in the range of 393–473 K and 303–393 K. For the first section, namely in the range of 0.0021–0.0025 K^{-1}, the fitting curve, as shown in Fig. 12(a), is highly matched with the experimental data, indicating the small error and high accuracy of the data. The absolute sensitivity S_a and relative sensitivity S_r were further derived and are portrayed in Fig. 12(b). Both S_a and S_r monotonically increase as the temperature increases from 393 K to 473 K. The maximum S_a and S_r at 473 K are 8.573% K^{-1} and 1.927% K^{-1}, respectively. The relatively large S_a is superior to most other materials for the application of a temperature sensor. Table 1 lists the S_a values of several other temperature measuring materials for comparison. This result suggests that the SGAO:0.04Bi^{3+},0.003Mn^{4+} phosphor is a promising temperature measuring material, particularly in the 393–473 K range.

In the temperature range of 303–393 K with the corresponding horizontal coordinate (1/T) range of 0.0025–0.0033 K^{-1}, the FIR ($I_{\mathrm{Mn}^{4+}}/I_{\mathrm{Bi}^{3+}}$) fitting curve (Fig. 12(c)) also exhibits a monotonical decreasing trend. Fig. 12(d) shows the S_a and S_r in the corresponding range. The maximum S_a and S_r are 0.172%

K^{-1} and 0.433% K^{-1} at 303 K, respectively. Obviously, the property in this range is depressingly not as good as that in the high-temperature range, which may have a certain adverse effect on its application.

4. Conclusion

In conclusion, a series of Bi^{3+} single-doped and Bi^{3+},Mn^{4+} co-doped SGAO phosphors were synthesized by the traditional high-temperature solid-phase method. The emission center of SGAO:Bi^{3+} is 404 nm. The optimal excitation wavelength and doping concentration are 300 nm and 4 at%, respectively. The concentration quenching effect is mainly caused by dipole–dipole interaction. With the concentration of Bi^{3+} kept constant at 4 at%, different contents of Mn^{4+} were co-doped and the optimized concentration was determined as 0.3 at%. Via the PL and EPL spectra, as well as the fluorescence lifetimes with different Mn^{4+} concentrations, the mechanism and efficiency of energy transfer between Bi^{3+} and Mn^{4+} were studied. The highest efficiency reaches 79.4%. To investigate the temperature sensing properties of the SGAO:0.04Bi^{3+},0.003Mn^{4+} phosphor, variational PL spectra were conducted in the temperature range of 303–473 K. The results show that SGAO:0.04-Bi^{3+},0.003Mn^{4+} phosphor exhibits wide, completely non-overlapping blue-purple and red emission bands under 300 nm excitation, which corresponds to the $^3P_1 \rightarrow {}^1S_0$ transition of Bi^{3+} and the $^2E_g \rightarrow {}^4A_{2g}$ transition of Mn^{4+}, respectively, providing beneficial conditions for the purpose of a temperature sensing application. Based on the comprehensive analysis, the SGAO:0.04Bi^{3+},0.003Mn^{4+} phosphor was demonstrated to possess high thermal detection sensitivity and good signal resolution, especially in the temperature range of 393–473 K. At 473 K, the S_a and S_r of the SGAO:0.04Bi^{3+},0.003Mn^{4+} phosphor are 8.573% K^{-1} and 1.927% K^{-1}, respectively, much better than those of most other reported optical temperature sensing materials. With all the analyses combined, it is reasonable to assert that the SGAO:0.04Bi^{3+},0.003Mn^{4+} phosphor is a prominent temperature sensing material that possesses properties of excellent signal resolution and accurate temperature detection.

Conflicts of interest

On behalf of all authors, the corresponding author states that there is no conflict of interest which could have appeared to influence the work reported in this paper.

Acknowledgements

References

1 Q. Wang, S. Zhao, J. Wen, X. X. Huang, C. L. Wei, Q. S. Xia, Z. F. Mu and H. Guo, A self-referenced fluorescence intensity ratio optical temperature sensing materials $K_3YSi_2O_7:Bi^{3+}/Sm^{3+}$ based on multi-strategy combination, *Ceram. Int.*, 2023, DOI: 10.1016/j.ceramint.2023.03.320.

2 B. F. Hou, M. C. Jia, P. P. Li, G. F. Liu, Z. Sun and Z. L. Fu, Multifunctional Optical Thermometry Based on the Rare-Earth-Ions-Doped Up-/Down-Conversion $Ba_2TiGe_2O_8$:Ln (Ln = $Eu^{3+}/Er^{3+}/Ho^{3+}/Yb^{3+}$) Phosphors, *Inorg. Chem.*, 2019, **58**, 7939–7946.

3 A. Q. Zhang, Z. Sun, G. F. Liu, Z. L. Fu, Z. D. Hao, J. H. Zhang and Y. L. Wei, Ln^{3+} (Er^{3+}, Tm^{3+} and Ho^{3+})-doped $NaYb(MoO_4)_2$ upconversion phosphors as wide range temperature sensors with high sensitivity, *J. Alloys Compd.*, 2017, **728**, 476–483.

4 Z. Sun, G. F. Liu, Z. L. Fu, Z. D. Hao and J. H. Zhang, A novel upconversion luminescent material: Li^+- or Mg^{2+}-codoped $Bi_{3.84}W_{0.16}O_{6.24}$: Tm^{3+}, Yb^{3+} phosphors and their temperature sensing properties, *Dyes Pigm.*, 2018, **151**, 287–295.

5 W. S. Silveira, P. A. M. Nascimento, A. J. S. Silva and M. V. S. Rezende, Luminescent properties and energy transfer mechanism from Tb^{3+} to Eu^{3+} doped in $Y_3Al_5O_{12}$ phosphors, *J. Alloys Compd.*, 2020, **822**, 153651.

6 R. F. Wei, J. L. Guo, K. J. Li, L. P. Yang, X. L. Tian, X. M. Li, F. F. Hu and H. Guo, Dual-emitting $SrY_2O_4:Bi^{3+},Eu^{3+}$ phosphor for ratiometric temperature sensing, *J. Lumin.*, 2019, **216**, 116737.

7 R. Kandan, A. Jain, P. Venkatesh and B. Prabhakara Reddy, Enthalpy measurements and thermodynamic properties of M_2TeO_6(s) (M = Eu, Dy), *J. Chem. Thermodyn.*, 2020, **144**, 106056.

8 D. R. Taikar, Study of energy transfer from Bi^{3+} to Tb^{3+} in Y_2O_3 phosphor and its application for W-LED, *J. Alloys Compd.*, 2020, **828**, 154405.

9 D. Xu, P. L. Yu and L. H. Tian, Luminescence properties of Pr^{3+} and Bi^{3+} co-doped $NaCaTiNbO_6$ phosphor for red-LEDs, *J. Rare Earths*, 2018, **36**, 243–247.

10 Y. Meng, Z. Z. Lu, S. Wang, H. Fan, L. Y. Zhou, L. Yang and C. Z. Zhong, Synthesis and luminescence properties of double perovskite Bi^{3+}/Mn^{4+} co-doped Ca_2GdTaO_6 phosphor, *J. Lumin.*, 2021, **233**, 117898.

11 J. Han, F. J. Pan, M. S. Molokeev, J. F. Dai, M. Y. Peng, W. J. Zhou and J. Wang, Redefinition of Crystal Structure and Bi^{3+} Yellow Luminescence with Strong Near-Ultraviolet Excitation in $La_3BWO_9:Bi^{3+}$ Phosphor for White Light-Emitting Diodes, *ACS Appl. Mater. Interfaces*, 2018, **10**, 13660–13668.

12 H. H. Zhang, Y. Y. Chen, X. Y. Zhu, K. L. Liu, H. C. Zhou, X. K. Sun, N. N. Li and Y. L. Feng, The deep red $Ca_2YZr_2Al_3O_{12}:Mn^{4+}$ phosphor and enhanced emission by Bi^{3+} doping, *J. Lumin.*, 2021, **236**, 118131.

13 Y. Zhang, X. J. Zhang, L. L. Zheng, Y. Zeng, Y. Lin, Y. L. Liu, B. F. Lei and H. R. Zhang, Energy transfer and tunable emission of $Ca_{14}Al_{10}Zn_6O_{35}:Bi^{3+},Sm^{3+}$ phosphor, *Mater. Res. Bull.*, 2018, **100**, 56–61.

14 Y. Y. Liu, J. Gao, W. Shi, X. Y. Feng, Z. J. Zhou, J. X. Wang, J. L. Guo, R. Y. Kang, B. Deng and R. J. Yu, Deep-red-emitting $Mg_2InSbO_6:Mn^{4+}$ phosphors with a double-perovskite structure for plant-cultivation LEDs: Synthesis and photoluminescence properties, *Ceram. Int.*, 2021, **47**, 18814–18823.

15 Z. Zhou, Y. Zhong, M. Xia, N. Zhou, B. F. Lei, J. Wang and F. F. Wu, Tunable dual emission of $Ca_3Al_4ZnO_{10}:Bi^{3+},Mn^{4+}$ via energy transfer for indoor plant growth lighting, *J. Mater. Chem. C*, 2018, **6**, 8914–8922.

16 F. Baur, T. Jansen and T. Jüstel, First report of energy transfer from uranyl to Mn^{4+} in $K_3(UO_2)F_5:Mn^{4+}$, *J. Lumin.*, 2021, **237**, 118085.

17 Y. Yu, K. Shao, C. H. Niu, M. J. Dan, Z. B. Wang, Y. Y. Wang, J. Chen, J. N. Luo, S. Y. Liu and Z. Xie, Ca^{2+} enhanced far-red emission performance and efficiency of $SrGd_2Al_2O_7:Mn^{4+}$ phosphor for the potential application in plant growth lighting, *J. Chem. Phys.*, 2023, **158**, 234703.

18 J. H. Ou, X. L. Yang and S. G. Xiao, Luminescence performance of Cr^{3+} doped and Cr^{3+}, Mn^{4+} co-doped La_2ZnTiO_6 phosphors, *Mater. Res. Bull.*, 2020, **124**, 110764.

19 H. Zhang, H. Yang, X. J. Ma, G. G. Li, S. Q. Liu, H. R. Li, J. Yang, Y. J. Liang and Y. J. Chen, Tunable dual emission of Bi^{3+} and Mn^{4+} co-doped $LaMg_{0.598}Nb_{0.402}O_3$ double perovskite via energy transfer for plant growth lighting, *Mater. Res. Bull.*, 2020, **126**, 110814.

20 Y. H. Xu, L. Zhang, L. P. Dong, S. W. Yin, X. D. Wu and H. P. You, Novel $SrGd_2Al_2O_7:Mn^{4+}$, Nd^{3+}, and Yb^{3+} phosphors for c-Si solar cells, *Dalton Trans.*, 2021, **50**, 7017–7025.

21 D. Y. Huang, P. P. Dang, H. Z. Lian, Q. G. Zeng and J. Lin, Luminescence and Energy-Transfer Properties in Bi^{3+}/Mn^{4+}-Codoped Ba_2GdNbO_6 Double-Perovskite Phosphors for White-Light-Emitting Diodes, *Inorg. Chem.*, 2019, **58**, 15507–15519.

22 P. P. Dang, D. J. Liu, G. G. Li, A. A. Al Kheraif and J. Lin, Recent Advances in Bismuth Ion-Doped Phosphor Materials: Structure Design, Tunable Photoluminescence Properties, and Application in White LEDs, *Adv. Opt. Mater.*, 2020, **8**, 1901993.

23 C. L. Wang, Y. H. Jin, L. F. Yuan, H. Y. Wu, G. F. Ju, Z. Z. Li, D. Liu, Y. Lv, L. Chen and Y. H. Hu, A spatial/temporal dual-mode optical thermometry platform based on synergetic luminescence of Ti^{4+}-Eu^{3+} embedded flexible 3D micro-rod arrays: High-sensitive temperature sensing and multi-

dimensional high-level secure anti-counterfeiting, *Chem. Eng. J.*, 2019, **374**, 992–1004.

24 C. D. S. Brites, P. P. Lima, N. J. O. Silva, A. Millan, V. S. Amaral, F. Palacio and L. D. Carlos, A Luminescent Molecular Thermometer for Long-Term Absolute Temperature Measurements at the Nanoscale, *Adv. Mater.*, 2010, **22**, 4499–4504.

25 C. D. S. Brites, R. Marin, M. Suta, A. N. C. Neto, E. Ximendes, D. Jaque and L. D. Carlos, Spotlight on Luminescence Thermometry: Basics, Challenges, and Cutting-Edge Applications, *Adv. Mater.*, 2023, 2302749; K. Kniec, W. Piotrowski, K. Ledwa, L. D. Carlos and L. Marciniak, Spectral and thermometric properties altering through crystal field strength modification and host material composition in luminescence thermometers based on Fe^{3+} doped AB_2O_4 type nanocrystals (A = Mg, Ca; B = Al, Ga), *J. Mater. Chem. C*, 2021, **9**, 517–527.

26 I. E. Kolesnikov, A. A. Kalinichev, M. A. Kurochkin, D. V. Mamonova, E. Y. Kolesnikov and E. Lahderanta, Ratiometric Optical Thermometry Based on Emission and Excitation Spectra of YVO_4:Eu^{3+} Nanophosphors, *J. Phys. Chem. C*, 2019, **123**, 5136–5143; Y. F. S. Wu, S. L. Xu, F. Q. Lai, B. Liu, J. H. Huang, X. Y. Ye and W. X. You, Intense near-infrared emission, upconversion processes and temperature sensing properties of Tm^{3+} and Yb^{3+} co-doped double perovskite Gd_2ZnTiO_6 phosphors, *J. Alloys Compd.*, 2019, **804**, 486–493.

27 A. M. Voiculescu, S. Hau, G. Stanciu, D. Avram and C. Gheorghe, Optical thermometry through infrared excited green upconversion emissions of Er^{3+}-Yb^{3+} co-doped $LaAlO_3$ phosphors, *J. Lumin.*, 2022, **242**, 118602.

28 M. Wu, D. G. Deng, F. P. Ruan, B. W. Chen, L. Lei, R. S. Lei and S. Q. Xu, Double-site emission of Eu^{2+} ions in $Sr_4Al_{14}O_{25}$:Eu^{2+} phosphors for self-calibrated optical thermometry, *Opt. Mater.*, 2019, **88**, 704–710.

29 B. j. Zhu, S. Q. Ren, Y. L. Liu, D. Zhang, Q. R. Wang, S. H. Li, B. Yang, W. J. Wang and B. Yang, Influence of Mn^{2+} ions on the structure, spectral characteristics and optical thermometry performances of $ZnAl_2O_4$:Cr^{3+} multifunctional phosphors, *J. Lumin.*, 2022, **244**, 118736.

30 X. Y. Li, G. C. Jiang, S. S. Zhou, X. T. Wei, Y. H. Chen, C. K. Duan and M. Yin, Luminescent properties of chromium(III)-doped lithium aluminate for temperature sensing, *Sens. Actuators, B*, 2014, **202**, 1065–1069.

31 Y. Ding, N. Guo, X. Lu, H. T. Zhou, L. Wang, R. Z. Ouyang, Y. Q. Miao and B. Q. Shao, None-rare-earth activated $Ca_{14}Al_{10}Zn_6O_{35}$:Bi^{3+},Mn^{4+} phosphor involving dual luminescent centers for temperature sensing, *J. Am. Ceram. Soc.*, 2019, **102**, 7436–7447.

32 M. X. Zhang, M. C. Jia, T. Q. Sheng and Z. L. Fu, Multifunctional optical thermometry based on the transition metal ions doped down-conversion Gd_2ZnTiO_6:Bi^{3+}, Mn^{4+} phosphors, *J. Lumin.*, 2021, **229**, 117653.